ZIBELINE INTERNATIONAL PUBLISHING

ISSN: 2716-7100 (Online)
CODEN: MCEMC2

Materials & Corrosion Engineering Management (MACEM)

DOI: http://doi.org/10.26480/macem.02.2020.35.38

RESEARCH ARTICLE

CRYSTALLIZATION PROCESSES OF SOME AMORPHOUS ALLOYS

W.Q. Yu[a], L.P. Lu[a,b*]

[a] ***School of Materials Science and Engineering, Changchun University of Science and Technology, Changchun 130022, China.***
[b] ***National Demonstration Center for Experimental Physics Education, Jilin Normal University, Siping 136000, China.***
****Corresponding Author E-mail: luliping771219@126.com***

ARTICLE DETAILS

Article History:

Received 15 May 2020
Accepted 20 June 2020
Available online 14 July 2020

ABSTRACT

A series of $Fe_{40}Co_{40}Zr_8M_2B_{10}$ (M=Nb, V, Cr, Ti, W, Al) alloys were prepared using melt-spinning. The thermal curve, structure and magnetic property of alloys are examined. Because of different negative heat of mixing between elements, only $Fe_{40}Co_{40}Zr_8M_2B_{10}$ (M=Nb, V, Cr, Ti) alloys form amorphous structure. These amorphous alloys are annealed at different temperatures under vacuum conditions. The crystallization processes of four amorphous alloys are similar. In the primary stage of crystallization process, only α-Fe (Co) phase precipitates and Co element mainly distributes in the residual amorphous. For the four alloys after annealing at 550℃, there is a few differences in saturation magnetization ($\boldsymbol{M_s}$) and coercivity ($\boldsymbol{Hc}$) due to their different microstructures.

KEYWORDS

amorphous alloys, microstructures, crystallization, thermal curve.

1. INTRODUCTION

Since the excellent soft magnetic properties, Fe-based nanocrystalline soft magnetic materials have been attracted lots of attentions for a long time. Among the Fe-based nanocrystalline soft magnetic alloys, Hitperm FeCoMB (Cu) alloys as competitive materials for high temperature soft magnetic applications have been developed and attracted lots of attentions in recent years (Han et al., 2014; Babu et al., 2011; Sun et al., 2009; Radon et al., 2018). The magnetism of the materials is closely related to their microstructures composed by α-FeCo nanocrystals embedded in amorphous matrix. Grain size is one of the important factor affecting the properties of nanocrystalline soft magnetic materials. Within the exchange correlation length, coercivity ($\boldsymbol{H_c}$) of nanocrystalline alloys with the two-phase structure follows a D^6 power law (Herzer, 1990). Moreover, $\boldsymbol{H_c}$ is also related to the grain-size distribution of α-Fe nanograins (Bitoh et al., 2003).

In order to improve the performance of alloys, a wide variety of elements have been added into Fe-based alloy system. Adding transition metal can greatly improve and adjust their microstructure and performance, such as Nb, V, Cr, Ti, W and Al element. Nb and W are the most effective elements which can refine the grain size during annealing treatment (Li et al., 2017; Alleg et al., 2012; Silveyra and Illekova, 2014; Ji et al., 2018; Ma et al., 2016; Botta et al., 2014; Xu et al., 2018; Liu et al., 2014; Wang et al., 2018; Yang et al., 2013; Liang et al., 2018; Stepanov et al., 2019; He et al., 2014; Duan et al., 2019; Murugaiyan et al., 2018; Takeuchi and Inoue, 2005). The addition of V can improve the amorphous forming ability and the bending ductility of the alloys (Ji et al., 2018). Minor Cr addition significantly improves the corrosion resistance (Liu et al., 2014). Doping Ti can decrease core loss mainly by reducing its hysteresis loss (Yang et al., 2013). Al doping results in the reduction of grain size and coercivity (Takeuchi and Inoue, 2005). In this paper, the $Fe_{40}Co_{40}Zr_8M_2B_{10}$ (M=Nb, V, Cr, Ti, W, Al) alloy system is based on the addition of different transition metals to a conventional Hitperm-like amorphous alloy system. The crystallization processes and magnetic properties of $Fe_{40}Co_{40}Zr_8M_2B_{10}$ alloys with different transition metal will be discussed in detail.

2. EXPERIMENTAL

2.1 Preparation

Ingots of $Fe_{40}Co_{40}Zr_8M_2B_{10}$ (M=Nb, V, Cr, Ti, W, Al) alloys were prepared by arc melting the mixtures of the pure metals above 99.9% and pure B (99.999%), and the ingots were remelted with the magnetic stirring for 4 times to ensure the homogeneity under vacuum conditions. Then alloy ribbons were prepared using a single roller melt-spinning equipment with copper wheel rotating at a surface velocity of 38 m/s. Ribbons were 1 cm in width and about 30 μm in thickness. $Fe_{40}Co_{40}Zr_8M_2B_{10}$ [M=Nb(#1), V(#2), Cr(#3), Ti(#4)] amorphous alloys were post annealed at 500, 550, 600, 650 and 700℃ for 1h under vacuum conditions, respectively.

2.2 Measurements

Thermal curves were performed by differential scanning colorimetry (DSC, Diamond) instrument. Structures of alloys were identified by transmission electron microscopy (TEM, JEM-2100E) and X-ray diffraction (XRD, D/max 2500/PC, 40 kV, 200 mA, Cu-Kα, λ=1.5406 Å). Thin-film TEM specimens were prepared by region ion beam thinning technique. Magnetic hysteresis loops were examined by vibrating sample magnetometer (VSM, Lake Shore M7407).

Quick Response Code	Access this article online	
	Website: https://macej.com.my	**DOI:** 10.26480/macem.02.2020.35.38

Cite the Article: W.Q. Yua, L.P. Lu (2020). Crystallization Processes Of Some Amorphous Alloys.
Materials & Corrosion Engineering Management, 1(2): 35-38.

3. RESULTS AND DISCUSSION

3.1 Glass forming ability of alloys

Figure 1 gives the XRD patterns of $Fe_{40}Co_{40}Zr_8M_2B_{10}$ (M=Nb, V, Cr, Ti, W, Al) alloys as quenched. $Fe_{40}Co_{40}Zr_8M_2B_{10}$ (M=Nb, V, Cr, Ti) alloys as quenched are all amorphous but not for $Fe_{40}Co_{40}Zr_8M_2B_{10}$ (M=W, Al) alloys.

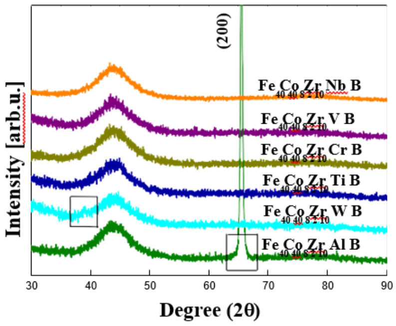

Figure 1: XRD patterns of Fe40Co40Zr8M2B10 (M=Nb, V, Cr, Ti, W, Al) alloys as-quenched.

Table 1 gives the values of the heat of mixing between M element and other elements (Inoue, 2000). For $Fe_{40}Co_{40}Zr_8W_2B_{10}$ alloy, the negative heat of mixing between W and other elements is relatively low. Therefore, $Fe_{40}Co_{40}Zr_8W_2B_{10}$ alloy is not fully amorphous. $Fe_{40}Co_{40}Zr_8Al_2B_{10}$ alloy has large negative heats of mixing between Al element and other elements. However, the (200) diffraction peak of α-Fe (Co) phase can be observed. It should be that Al has a large saturation vapor pressure and evaporates during the smelting process. For $Fe_{40}Co_{40}Zr_8M_2B_{10}$ (M=Nb, V, Cr, Ti) alloys, the negative heat of mixing between M(M=Nb, V, Cr, Ti) and other elements are bigger and form amorphous structure in the as-quenched state.

Table 1: The values of heat of mixing between M and other elements (kJ/mol).

M	Fe	Co	Zr	B
Nb	-16	-25	4	-54
V	-7	-14	-4	-42
Cr	-1	-4	-12	-31
Ti	-17	-28	0	-58
W	0	-1	-9	-31
Al	-11	-19	-44	0

For the as-quenched alloys which is not fully amorphous, the existing grains will increase rapidly after heat treatment, resulting in the great difference in grain size. Relatively uniform grains can be obtained by annealing amorphous alloys. Therefore, we mainly study the crystallization processes and magnetic properties of $Fe_{40}Co_{40}Zr_8M_2B_{10}$ (M=Nb, V, Cr, Ti) amorphous alloys. DSC traces of $Fe_{40}Co_{40}Zr_8M_2B_{10}$ (M=Nb, V, Cr, Ti) alloys as-quenched are shown in figure 2. The glass forming ability (GFA) can be calculated by the temperature span of the super-cooled liquid region ΔT_x (difference between T_g and T_x) (Yu et al., 2017). The glass transition temperature (T_g), onset crystallization temperature (T_x), super-cooled liquid region ΔT_x and crystallization peak temperature (T_p) can be obtained by DSC.

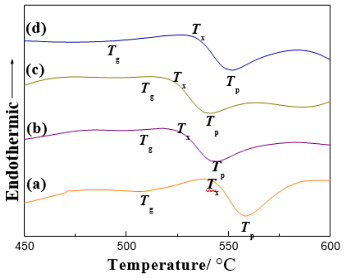

Figure 2: DSC traces of four amorphous alloys at a heating rate of 10°C /min; (a)$Fe_{40}Co_{40}Zr_8Nb_2B_{10}$, (b) $Fe_{40}Co_{40}Zr_8V_2B_{10}$; (c) $Fe_{40}Co_{40}Zr_8Cr_2B_{10}$, (d) $Fe_{40}Co_{40}Zr_8Ti_2B_{10}$

Table 2 gives a list of T_g, T_x, ΔT_x and T_p of four kinds of amorphous alloys. The wider the ΔT_x is, the greater the GFA is. Both ΔT_x and T_p of the alloys have the following relations: $\Delta T_{x\#4} > \Delta T_{x\#1} > \Delta T_{x\#2} > \Delta T_{x\#3}$ and $T_{p\#1} > T_{p\#4} > T_{p\#2} > T_{p\#3}$. The GFA of four amorphous alloys has the following relations: $GFA_{\#4} > GFA_{\#1} > GFA_{\#2} > GFA_{\#3}$. The negative heat of mixing between M (M=Nb, V, Cr, Ti) and other elements have the following relations: $H_{\#4} > H_{\#1} > H_{\#2} > H_{\#3}$. Therefore, the GFA of four kinds of alloy presents the results above.

Table 2: T_g, T_x, ΔT_x and T_p of $Fe_{40}Co_{40}Zr_8M_2B_{10}$ (M=Nb, V, Cr, Ti) amorphous alloys.

	$Fe_{40}Co_{40}Zr_8Nb_2B_{10}$ (#1)	Fe40Co40Zr8V2B10 (#2)	$Fe_{40}Co_{40}Zr_8Cr_2B_{10}$ (#3)	$Fe_{40}Co_{40}Zr_8Ti_2B_{10}$ (#4)
T_g/°C	505.0	505.5	506.3	496.8
T_x/°C	540.1	524.7	522.2	532.6
ΔT_x/°C	35.1	19.2	15.9	35.8
T_p/°C	558.3	543.0	539.6	551.7

3.2 Crystallization processes of alloys

XRD patterns of $Fe_{40}Co_{40}Zr_8M_2B_{10}$ (M=Nb, V, Cr, Ti) alloys after annealing are shown in figure 3. The crystallization processes of these four amorphous alloys are similar. After annealing at 500℃ , only α-Fe(Co) phase is formed. The lattice constants of α-Fe (Co) of $Fe_{40}Co_{40}Zr_8M_2B_{10}$ (M=Nb, V, Cr, Ti) alloys after annealing at 550℃ are 2.860, 2.859, 2.860 and 2.862, respectively. The lattice constants of pure α-FeCo and α-Fe are 2.8550 and 2.8664 Å, respectively (Yu et al., 2017). It is deduced that Co element in the alloys mainly distributes into the remained amorphous. It is attributed to the big heat of mixing between Co element and Zr element (-41 kJ/mol). More and more α-Fe (Co) nanocrystals precipitate and the diffraction peaks intensity increases with the increase of annealing temperature. After annealing at 650℃ , $ZrCo_3B_2$ phase forms. The precipitation of $ZrCo_3B_2$ phase at high temperature is due to that the Co element in residual amorphous matrix reacts with the Zr and B elements distributed in the residual amorphous matrix. The crystalline phases of alloys precipitated at the final annealing stage are the same and identified to be α-Fe(Co), $ZrCo_3B_2$ and $Fe(Co)_3Zr$ phases. The crystallization processes of these four amorphous alloys are similar: amorphous→remained amorphous+α-Fe(Co)→α-Fe(Co)+$ZrCo_3B_2$+$Fe(Co)_3Zr$.

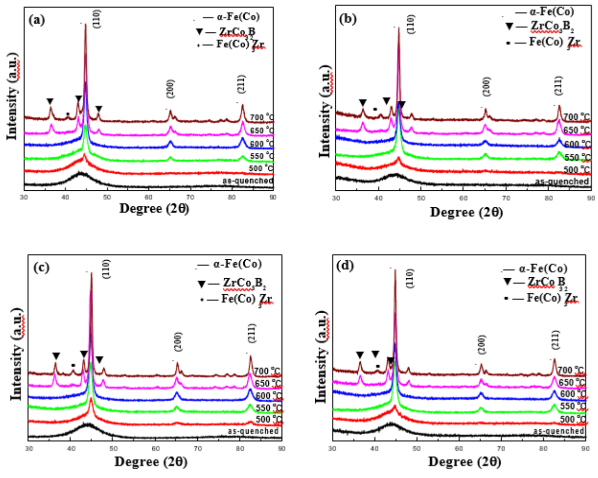

Figure 3: XRD patterns of four kinds of alloys after annealing at different temperatures. (a) $Fe_{40}Co_{40}Zr_8Nb_2B_{10}$, (b) $Fe_{40}Co_{40}Zr_8V_2B_{10}$, (c) $Fe_{40}Co_{40}Zr_8Cr_2B_{10}$, (d) $Fe_{40}Co_{40}Zr_8Ti_2B_{10}$.

Figure 4 shows the TEM images, SAED patterns and PSD of the alloys after annealing at 550℃. For the four kinds of alloys after annealing at 550℃, the nanocrystals are surrounded by a residual amorphous matrix. SAED patterns all show the crystallization phase is only α-Fe(Co). They all form a typical two-phase structure characterized by bcc α-Fe(Co) nanocrystalline grains embedding in the amorphous matrix. The volume fraction of $Fe_{40}Co_{40}Zr_8Nb_2B_{10}$ alloy is the lowest and the crystallization volume fraction of $Fe_{40}Co_{40}Zr_8Cr_2B_{10}$ alloy is the biggest. The crystallization volume fraction of $Fe_{40}Co_{40}Zr_8M_2B_{10}$ (M=Nb, V, Cr, Ti) alloys have the following relations:$V_{\#3}>V_{\#2}>V_{\#4}>V_{\#1}$. According to the grain size distribution, the grain size [α-Fe(Co)] of $Fe_{40}Co_{40}Zr_8M_2B_{10}$ (M=Nb, V, Cr, Ti) alloys are 7.8, 7.2, 6.9 and 8.2 nm, respectively. Furthermore, $Fe_{40}Co_{40}Zr_8V_2B_{10}$ and $Fe_{40}Co_{40}Zr_8Ti_2B_{10}$ alloys nanocrystals distribute inhomogeneously. During the annealing process of amorphous alloy, the transition metal will reject from α-Fe particles and accumulate in the residual amorphous matrix, thus reducing the growth of α-Fe particles. The difference in the atomic radius and electronegative between elements leads to the differences in grain refinement.

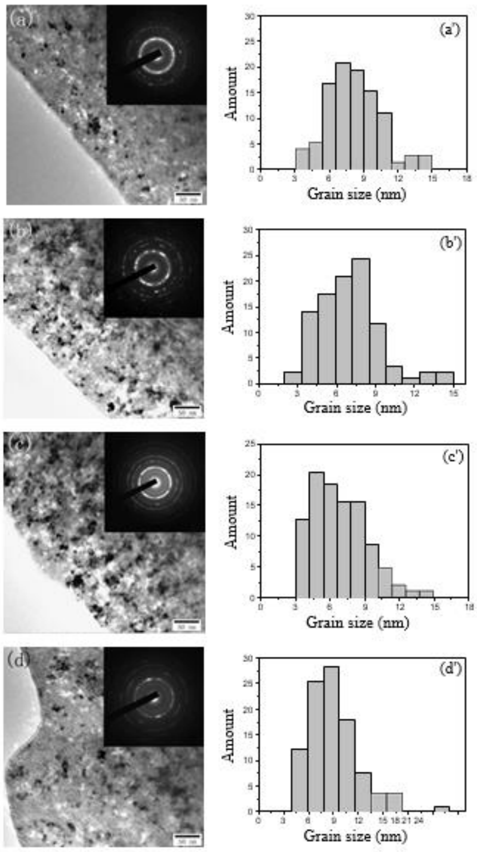

Figure 4: Left is the transmission electron microscope (TEM) images and selected-area electron diffraction (SAED) patterns of the alloys after annealing at 550°C ; Right is the grain size distribution (PSD) of the alloys after annealing at 550°C . (a, a')$Fe_{40}Co_{40}Zr_8Nb_2B_{10}$, (b, b') $Fe_{40}Co_{40}Zr_8V_2B_{10}$, (c, c') $Fe_{40}Co_{40}Zr_8Cr_2B_{10}$, (d, d') $Fe_{40}Co_{40}Zr_8Ti_2B_{10}$

3.3 Magnetic properties of alloys

The magnetic hysteresis loops of $Fe_{40}Co_{40}Zr_8M_2B_{10}$ (M=Nb, V, Cr, Ti) alloys are shown in figure 5. Four kinds of alloys all show good soft magnetic property from magnetic hysteresis loops. Table 3 gives the saturation magnetization (M_s) and coercivity (H_c) of $Fe_{40}Co_{40}Zr_8M_2B_{10}$ (M=Nb, V, Cr, Ti) alloys annealed at 550°C.

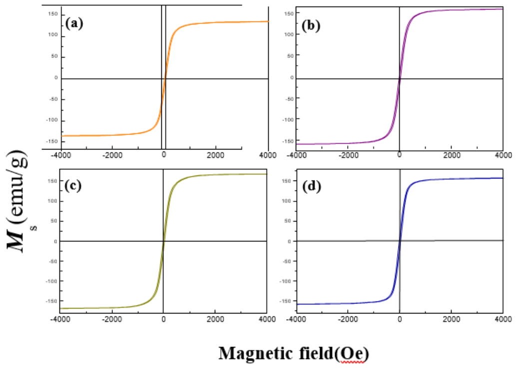

Figure 5: Magnetic hysteresis loops of $Fe_{40}Co_{40}Zr_8M_2B_{10}$ (M=Nb, V, Cr, Ti) alloys annealed at 550℃;(a)$Fe_{40}Co_{40}Zr_8Nb_2B_{10}$, (b) $Fe_{40}Co_{40}Zr_8V_2B_{10}$, (c) $Fe_{40}Co_{40}Zr_8Cr_2B_{10}$, (d) $Fe_{40}Co_{40}Zr_8Ti_2B_{10}$

Table 3: Ms and Hc of Fe40Co40Zr8M2B10 (M=Nb, V, Cr, Ti) alloys

	M_s (emu/g)	Hc (Oe)
$Fe_{40}Co_{40}Zr_8Nb_2B_{10}$ (#1)	135.4	22.4
$Fe_{40}Co_{40}Zr_8V_2B_{10}$ (#2)	159.0	24.6
$Fe_{40}Co_{40}Zr_8Cr_2B_{10}$ (#3)	169.0	22.5
$Fe_{40}Co_{40}Zr_8Ti_2B_{10}$ (#4)	158.3	24.5

There is a little difference in Coercivity (H_c) among alloys, which is due to the different grain size and different nanocrystals distribution of α-Fe(Co) phase. The differences in saturation magnetization (M_s) among alloys is due to the differences of crystallization volume fraction of α-Fe (Co) phase. M_s of the alloys has the following relations: $M_{s\#3}> M_{s\#2}> M_{s\#4}> M_{s\#1}$.

4. CONCLUSION

$Fe_{40}Co_{40}Zr_8M_2B_{10}$ (M=Nb, V, Cr, Ti, W, Al) alloys were prepared by melt-spinning. Among of them, $Fe_{40}Co_{40}Zr_8M_2B_{10}$ [M=Nb(#1), V(#2), Cr(#3), Ti(#4)] alloys have large negative heat of mixing and form amorphous. The GFA of the four kinds of alloy has the following relations: $GFA_{\#4}> GFA_{\#1}> GFA_{\#2}> GFA_{\#3}$. Only α-Fe(Co) phase precipitates in the primary stage of crystallization process and Co element mainly distributes into the residual amorphous. They all form a typical two-phase structure characterized by bcc α-Fe(Co) nanocrystalline grains embedding in the amorphous matrix. For the four amorphous alloys after annealing at 550℃ , there is a few differences in saturation magnetization (M_s) and coercivity (H_c) due to their different microstructures.

REFERENCES

Alleg, S., Souilah, S., Younes, A., Bensalem, R., Suñol, J.J., Greneche, J.M., 2012. Effect of the Nb content on the amorphization process of the mechanically alloyed Fe–Co–Nb–B powders. Journal of Alloys and Compounds, 536, Pp. S394-S397.

Babu, D.A., Majumdar, B., Sarkar, R., Raja, M.M., Akhtar, D., 2011. Nano crystallization of amorphous (Fe1-xCox)88Zr7B4Cu1 alloys and their soft magnetic properties. J. Mater. Research, 26, Pp. 2065-2071.

Bitoh, T., Makino, A., Inoue, A., Masumoto, T., 2003. Random Anisotropy Model for Nanocrystalline Soft Magnetic Alloys with Grain-Size Distribution. Materials Transactions, 44 (10), Pp.2011-2019

Botta, W.J., Berger, J.E., Kiminami, C.S., Roche, V., Nogueira, R.P., Bolfarini, C., 2014. Corrosion resistance of Fe-based amorphous alloys. Journal of Alloys and Compounds, 586 (1), Pp. S105-S110.

Duan, H., Wang, Z., Jia, Y., 2019. Al addition effect on structure and magnetic properties in high BS Fe-Cu-Si-B alloys. Materials Research Bulletin, 111, Pp. 289-293.

Han, B.K., Kim, Y.K., Choi-Yim, H., 2014. Effect of compositional variation on the soft magnetic properties of Fe(87−x−y) CoxTi7 Zr6By amorphous ribbons. Current Applied Physics, 14 (5), Pp. 685-687.

He, J.Y., Liu, W.H., Wang, H., Wu, Y., Liu, X.J., Nieh, T.J., Lu, Z.P., 2014. Effects of Al addition on structural evolution and tensile properties of the FeCoNiCrMn high-entropy alloy system. Acta Materialia, 62, Pp. 105-113.

Herzer, G., 1990. Grain size dependence of coercivity and permeability in nanocrystalline ferromagnets. IEEE Transactions on Magnetics, 26 (5), Pp. 1397-1402.

Inoue, A., 2000. Stabilization of metallic supercooled liquid and bulk amorphous alloys. Acta Materialia, 48 (1), Pp. 279-306.

Ji, L., Zheng, Z., Qiu, Z., Zeng, D., Yu, H., Xu, B., 2018. Effect of V addition on the performance of Fe73.5Cu1B13Si9.5Nb3-xVx soft magnetic alloys. Journal of Alloys and Compounds, 766, Pp.391-397.

Li, X., Liu, J., Qu, C., Song, K., Wang, L., 2017. Effects of Nb on the precipitation of α-Fe, glass forming ability and magnetic properties of Fe85B10P5 alloys. Journal of Alloys and Compounds, 694, Pp. 643-646.

Liang, D.D., Wei, X.S., Chang, C.T., Li, J.W., Wang, X.M., Shen, J., 2018. Effect of W addition on the glass forming ability and mechanical properties of Fe-based metallic glass. Journal of Alloys and Compounds, 731, Pp. 1146-1150.

Liu, W.L., Wang, Y.G., Chen, F.G., 2014. Effect of Ti on glass-forming ability and magnetic properties of Fe81Si4B12−x P2Cu1Ti x (x = 0–3) soft magnetic alloys. Journal of Materials Science: Materials in Electronics, 25, Pp. 5066–5070.

Ma, Y., Liu, Y., Li, J., Zhang, H., Yang, H., 2016. Effect of Alloying Method on Microstructure and Wear Resistance of Fe-Cr-V-B Based Alloy. Journal of Iron and Steel Research International, 23, Pp. 625–632

Murugaiyan, P., Abhinav, A., Verma, R., Panda, A.K., Mitra, A., Baysakh, S., Roy, R.K., 2018. Influence of Al addition on structural, crystallization and soft magnetic properties of DC Joule annealed FeCo based nanocrystalline alloys. Journal of Magnetism and Magnetic Materials, 448, Pp. 66-74.

Radoń, A., Włodarczyk, P., Hawełek, L., Gaweł, M.K., Gębara, P., Nowosielski, R., Babilas, R., 2018. Thermodynamic approach for determining chemical composition of Fe-Co based amorphous alloys with high thermal stability and glass forming ability. Journal of Alloys and Compounds, 763, Pp. 141-152.

Silveyra, J.M., Illeková, E., 2014. Effects of air annealing on Fe–Si–B–M–Cu (M = Nb, Mo) alloys. Journal of Alloys and Compounds, 610, Pp. 180-183.

Stepanov, N.D., Shaysultanov, D.G., Chernichenko, R.S., Tikhonovsky, M.A., Zherebtsov, S.V., 2019. Effect of Al on structure and mechanical properties of Fe-Mn-Cr-Ni-Al non-equiatomic high entropy alloys with high Fe content. Journal of Alloys and Compounds, 770, Pp. 194-203.

Sun, Y., Zhong, L., Bi, X., 2009. High temperature soft magnetic property of the nanocrystalline Fe44Co44Zr7B5 alloy arising from Ge addition. Scripta Materialia, 60 (9), Pp. 814-817.

Takeuchi, A., Inoue, A., 2005. Classification of Bulk Metallic Glasses by Atomic Size Difference, Heat of Mixing and Period of Constituent Elements and Its Application to Characterization of the Main Alloying Element. Materials Transactions, 46 (12), Pp. 2817-2829.

Wang, J., Liu, X., Mo, J., Mao, X., Fan, X., Luo, Z., 2018. The influence of doping Ti on the microstructure and magnetic performances of Fe-6.5Si soft magnetic composites. Journal of Alloys and Compounds, 766, Pp. 769-774.

Xu, D.D., Zhou, B.L., Wang, Q.Q., Zhou, J., Yang, W.M., Yuan, C.C., Xue, L., Fan, S.D., Ma, L.Q., Shen, B.L., 2018. Effects of Cr addition on thermal stability, soft magnetic properties and corrosion resistance of FeSiB amorphous alloys. Corrosion Science, 138, Pp. 20-27.

Yang, Z.J., Li, J., Linghu, R.F., Cheng, X.L., Yang, X.D., 2013. First-principle investigations on the structural dynamics of Ti2GaN. Journal of Alloys and Compounds, 574, Pp. 573-579.

Yu, W., Zeng, H., Sun, Y., Hua, Z., 2017. Effect of Mo addition on the thermal stability, microstructure and magnetic property of FeCoZrBCu alloys. Vacuum, 137, Pp. 175-182.

Yu, W., Zeng, H., Sun, Y., Sun, Y., Hua, Z., 2017. Effect of heating rates on the crystallization process of Fe64Co16Zr10B10 amorphous alloy. Physics Letters A, 381 (18), Pp. 1573-1576

Cite the Article: W.Q. Yua, L.P. Lu (2020). Crystallization Processes Of Some Amorphous Alloys.
Materials & Corrosion Engineering Management, 1(2): 35-38.